R. Nivethana KUMAR[,1] S. Muthu KUMARAN[,1] Vasudevan RAGHAVAN[1]

Numerical analysis of structure, stability and entropy generation in biogas coflow diffusion flames

Biogas is a gaseous biofuel predominantly composed of methane and carbon-dioxide. Stability of biogas flames strongly depend upon the amount of carbon-dioxide present in biogas, which varies with the source of biomass and reactor. In this paper, a comprehensive study on the stability and flame characteristics of coflow biogas diffusion flames is reported. Numerical simulations are carried out using reactive flow module in OpenFOAM, incorporated with variable thermophysical properties, Fick's and Soret diffusion, and short chemical kinetics mechanism. Effects of carbon-dioxide content in the biogas, temperatures of the fuel or coflowing air streams (preheated reactant) and hydrogen addition to fuel or air streams are analyzed. Entropy generation in these flames is also predicted. Results show that the flame temperature increases with the degree of preheat of reactants and the flames show better stability with the preheated air stream. Preheating the air contributes to increased flame stability and also to a significant decrease in entropy generation. Hydrogen addition, contributing to the same power rating, is seen to be relatively more effective in increasing the flame stability when added to the fuel stream. Results in terms of flow, temperature, species and entropy fields, are used to describe the stability and flame characteristics.

Nomenclature

a_{pi} — Planck mean absorption coefficient for species i, atm^{-1}m^{-1}
g — acceleration due to gravity, m/s^2
h — enthalpy, J/kg
h_i — enthalpy of species i, J/kg

✉ Vasudevan Raghavan, e-mail: raghavan@iitm.ac.in

[1]Department of Mechanical Engineering, Indian Institute of Technology Madras, Chennai – 600036, India.

J_i	species diffusion flux, kg/(m^{2}s)
k	thermal conductivity, W/(m K)
$M_{w,i}$	molecular weight of the species i, kg/kmol
p	pressure, N/m^2
p_i	partial pressure of species i, N/m^2
q_{rad}	volumetric radiative heat loss term, W/m^3
R_u	universal gas constant, kJ/(kmol K)
s_i	entropy, J/(kg K)
T	temperature, K
V	mixture velocity, m/s
$\bar{W}$	average molecular weight, kg/kmol
X_i	mole fraction of species i
Y_i	mass fraction of species i
$\Delta h^o_{f,i}$	enthalpy of formation of species i, J/kg
$\mu_{c,i}$	chemical potential, J/kg
ρ	density, kg/m^3
σ	Stefan-Boltzmann constant, $(5.67 \cdot 10^{-8}$ W/(m^{2}K^4))
τ	fluid stress tensor, N/m^2
$\dot{\omega}^m_i$	net reaction rate of species i, kg/(m^{3}s)

1. Introduction

The usage of alternative renewable fuels has increased recently due to the depletion, non-renewability and emission of greenhouse gases from conventional fossil fuels. Due to its widespread availability and superior emission characteristics, biogas is considered as a viable alternative fuel. Biogas is a renewable fuel formed from the anaerobic digestion of biomasses such as animal, plant and food waste. The major constituents of biogas are methane and carbon dioxide; besides these, water vapor, nitrogen and other small compounds are present in trace amounts. Depending upon the amount of CO_2, biogas flames can have stability issues in conventional burners. Therefore, it is necessary to investigate the structure of biogas flames and their stability for proper design of its burners.

The amount of CO_2 present in biogas varies depending upon the biomass source, climate and environment, which prevails during its production. There are several works in the literature reporting the composition of biogas produced from various sources. Recebli et al. [1] produced biogas ($CH_4 - 62\%$) through anaerobic fermentation reaction of animal manure. Rasi et al. [2] and Jonsson et al. [3] analysed the composition of biogas produced from landfills, sewage digester and organic wastes. They found that biogas obtained from the sewage digester plant has 35% to 45% of CO_2 and 55% to 65% of CH_4. Biogas got from landfills contain 30% to 40% of CO_2 and 45% to 55% of CH_4 and that from organic wastes contains 30% to 40% of CO_2 and 60% to 70% of CH_4. Therefore, the average composition of biogas obtained from production plants contains around 55% to 70% methane and

30% to 45% CO_2, besides trace amounts of nitrogen, ammonia, hydrogen sulfide, sulfur and organic silicon compounds. Khan et al. [4] reviewed the technologies for upgrading, utilization and storage of biogas. It was found that the biogas blended with Compressed Natural Gas (bio-CNG) can be a good substitute for conventional fuels used in vehicles, as it emits less pollutants.

Nonaka and Pereire [5] conducted experimental and numerical studies on the effect of addition of CO_2 in premixed biogas-air flames. The flame speed and adiabatic flame temperature decreased with increase in CO_2 content. They also found that the effect of CO_2 in the reaction $CO + OH \leftrightarrow CO_2 + H$ plays an important role in determining the flame structure. Abdallah et al. [6] experimentally studied the biogas characteristics for different CO_2 content, equivalence ratios and power rating. Stability maps were plotted for several biogas compositions as functions of Reynolds number (Re) and equivalence ratio. Zhang et al. [7] investigated the effect of CO_2 on methane-air flames. The addition of CO_2 increased the OH and decreased the CH concentrations in flames. They observed a change in the oxidation pathway of CH_4 with the addition of CO_2.

The stability of biogas can be improved by mixing it with fuels such as hydrogen. The high flame temperature and mass diffusivity of hydrogen widens the stability regimes of biogas flames. Leung and Wierzba [8] conducted experimental studies on the effect of H_2 addition on flame stability of biogas-air diffusion flames in coflowing air stream. The effect of nozzle jet diameter on the flame stability was also studied. They found that the blow-off limit significantly increased with hydrogen addition up to 10% (by volume). The enhancement in blow-off limit declined when hydrogen is increased continuously from 10% to 25% due to the slower reaction rate of methane which cannot be improved further with H_2 addition. With 30% hydrogen addition, the H_2 reactions dominated over the slow methane reactions and the blow-off limits increased significantly. The velocity range for stable flames also increased with an increasing hydrogen content and an increase in the nozzle jet diameter. Verma et al. [9] analysed the effect of hydrogen enrichment on biogas-biodiesel dual fuel engine. The efficiency increased with 20% hydrogen addition at high load. Further, a high reduction in CO (around 50%) and HC (around 35%) emissions were observed at low engine load.

Zhen et al. [10] experimentally studied the flame stability and heat transfer characteristics of biogas diffusion flame. The addition of hydrogen in CH_4-CO_2 mixture increased the blow off limits. They also studied the comparison of CH_4–CO_2 and CH_4-N_2 flames and found that the CO_2 diluted fuel displayed low stability limit, lower flame temperature and also lesser soot emission than the CH_4–N_2 flame. Zhen et al. [11] experimentally investigated the stability of biogas diffusion flames by increasing the level of hydrogen up to 25% (by volume). They observed that the blow-off velocity increased exponentially whereas the laminar flame speed increased linearly with hydrogen addition. The hydrogen addition accelerated the mass diffusion of fuel mixture, which improved the flame stability. A new scale law was obtained to predict the blow-off velocity of biogas-H_2 flames. Zhen et

al. [12] further analysed the stability and emission characteristics of premixed biogas-H_2-air flames. It was found that the flame stability was the best at an equivalence ratio of 1.2 and emission of CO reduced with an increase in hydrogen addition. It also extended the flammability limits of the mixture. Charest et al. [13] experimentally and numerically studied the effects of pressure on soot formation and flame temperature in simulated biogas (CH_4-CO_2) flames. The soot formation tendency with pressure increased with CO_2 concentration in biogas. It was also found that, at low pressures, an increase in the CO_2 content suppressed the soot formation. Wei et al. [14] experimentally studied the effect of CO_2 and hydrogen fractions on the heat transfer characteristics of impinging biogas-H_2 flames at an equivalence ratio of 1.2. It was observed that the total heat transfer rate from the impinging flame increased with hydrogen addition and the optimum amount of H_2 addition was about 30% by volume.

Mameri and Tabet [15] numerically studied the biogas-H_2 counterflow diffusion flames and observed an increase in the maximum temperature, mass fractions of OH, H and NO, with a decrease in CO_2 and hydrogen content. It was also found that the biogas-H_2 flames are more resistive to strain rates than pure biogas flames. At higher scalar dissipation rates, the biogas-H_2 flames emits lesser NO_x. Hence, practical burners operated at higher scalar dissipation rates (>50 s^{-1}) produced lesser NO_x emissions. Li et al. [16] measured the flame height, lift-off height, blowout velocities of biogas-air diffusion flames by varying the fuel mass fraction and preheat air temperatures. Their study revealed that the blowout velocity of preheated biogas flame was much higher as compared to normal diffusion flames. Prabhu et al. [17] reported from their experimental studies that preheated biogas-air mixture at the intake improved the brake thermal efficiency and reduced the brake fuel consumption in a dual fuel powered diesel engine. Moghaasi et al. [18] studied the effect of preheating and CO_2 dilution on oxy-MILD natural gas flames. With addition of CO_2, a uniform temperature distribution was observed, however, CO emissions notably increased. Further, with an increase in inlet temperature, CO formation through heavier hydrocarbons path ($C_2H_2 \rightarrow$ CO) was suppressed. The stability maps for biogas-air cross-flow flames, without and with obstacles were also reported [19].

Tsatsarnois et al. [20] numerically estimated the exergy destruction in an open gas turbine combustion system. They found that large exergy destruction was caused due to chemical reactions and heat transfer as compared to friction and mixing processes. Datta [21] numerically studied the rate of entropy generation in a confined axisymmetric laminar diffusion flame. The effects of inlet air temperature and air fuel ratio on the rate of entropy generation were studied using single step global reaction mechanism. It was observed that the total rate of entropy generation decreases with increase in air inlet temperature. The entropy generated due to mass transfer alone increased slightly with increase in air inlet temperature whereas the entropy generation due to heat transfer and chemical reactions decreased with air preheat. Saqr and Wahid [22] studied the effect of hydrogen addition on the

entropy generation in swirl stabilized methane flames. It was found that the rate of entropy generation increased with the addition of hydrogen to methane diffusion flames due to the irreversibility caused by heat transfer. Arjmandi and Amani [23] numerically investigated the entropy generation in swirl stabilized gas turbine combustor. A parametric study was done to calculate the entropy generation by varying the equivalence ratio, bluff-body size ratio, swirl number, fuel flow rate and air inlet velocity. They also emphasized that a trade-off must be achieved between entropy generation due to chemical reactions and heat transfer for optimum design of the combustor. Briones et al. [24] studied the hydrogen blended methane triple flame for analysing the entropy generation. They found that the addition of hydrogen to methane increased the entropy generation of the system due to increased heat transfer and the chemical reactivity, whereas the second law efficiency remained the same with hydrogen addition. Nishida et al. [25] studied the exergy loss and the entropy generation for methane and hydrogen fuels. The major contribution of total entropy generation was due to chemical reactions in a premixed flame and due to heat transfer in a diffusion flame. For premixed flames, the rate of entropy generation decreased on increasing the mixture temperature. Further, it was observed that the entropy generated due to chemical reaction were higher in flames fuelled by hydrogen as compared to methane. Wang et al. [26] analysed the entropy generation and exergy losses from hydrogen enhanced methane premixed flame in a micro-planar combustor. The authors observed a reduction in the entropy generation due to heat conduction and mass diffusion whereas the change in entropy generation due to chemical reactions was almost negligible.

From the above literature survey, it is clear that the stability of biogas flames has been extensively analysed. Many studies also report stability maps for stable operating range in different burners. However, inherent flame characteristics, temperature, flow, species and reactions fields in biogas flames have not been extensively studied. Further, the effect of preheated reactants on biogas flames in coflow configuration has not been investigated systematically. Hydrogen is mixed with several fuels to improve flame stability. The study on the effects of hydrogen addition to fuel and air streams in biogas flames is also scarce. These gaps in literature motivates the present study.

In this work, structure and stability of coflow non-premixed biogas-air flames of three biogas compositions, namely, BG30 (30% CO_2 – 70% CH_4), BG37.5 (37.5% CO_2 – 62.5% CH_4) and BG45 (45% CO_2 – CH_4) have been numerically studied. The range of CO_2 percent is selected based on the values obtained in biogas generation processes. The effects of preheated fuel or air on the flame stability are analysed by systematically varying the temperature of the fuel or the air streams. Similarly, the effect of hydrogen addition is investigated by adding some amount of H_2 either to the fuel stream or to the air stream on a given energy basis (% energy contributed by hydrogen kept less than 10% of the total energy). The entropy generated due to various processes such as heat transfer, chemical reactions, mass transfer, and coupled heat and mass transfer, are predicted for all the simulated

cases. Short chemical kinetics mechanism (25 species, 121 reaction steps), variable thermal and physical properties, Fick's diffusion and thermal diffusion (Soret effect) are incorporated in reactive flow module of OpenFOAM to numerically simulate various cases. The flame stability and structure of these flames are explained using temperature, flow, species and entropy generation fields, which are not easy to obtain by even sophisticated experimental measurements.

2. Numerical model and methodology

Numerical simulations are carried out using OpenFOAM. The governing equations for solving reactive flow, in a vector form, are presented below.

Continuity equation

$$\frac{\partial \rho}{\partial t} + \nabla \cdot \left(\rho \vec{V} \right) = 0 \,. \tag{1}$$

Momentum equation

$$\frac{\partial \left(\rho \vec{V} \right)}{\partial t} + \nabla \cdot \left(\rho \vec{V} \vec{V} \right) = -\nabla p + \nabla \cdot \vec{\tau} + \rho \vec{g}. \tag{2}$$

Species equation

$$\frac{\partial (\rho Y_i)}{\partial t} + \nabla \cdot \left(\rho \vec{V} Y_i \right) + \nabla \cdot \vec{J}_i = \dot{\omega}_i''' \,. \tag{3}$$

Energy equation

$$\frac{\partial (\rho h)}{\partial t} + \nabla \cdot \left(\rho \vec{V} h \right) = \nabla \cdot (k \nabla T) - \nabla \cdot \left[\sum_{i=1}^{n} h_i \vec{J}_i \right] - \sum_{i=1}^{n} \dot{\omega}_i''' \Delta h_{f,i}^o + \dot{q}_{\text{rad}}''' \,. \tag{4}$$

Thermal radiation absorbed by species such as CH_4, CO, CO_2 and H_2O, has been modelled using optically thin approximation-based model as reported by Barlow et al. [27]. Here, thermal energy radiated per unit volume (W/m^3) is expressed as,

$$\dot{q}_{\text{rad}}''' = 4\sigma \left(T^4 - T_b^4 \right) \sum \left(p_i \times a_{pi} \right) \,. \tag{5}$$

Equation (5) has been implemented as a volumetric sink term in the energy equation.

The species diffusion flux, $\vec{J}_i$, is calculated by considering mass diffusion (due to concentration gradient) and thermal or Soret diffusion (due to temperature gradient) as,

$$\vec{J}_i = -\rho D_{i,m} \nabla Y_i - D_{T,i} \frac{\nabla T}{T} \,, \tag{6}$$

where $D_{i,m}$ is the multi-component mass diffusion coefficient (m^2/s) for species i in the mixture and $D_{T,i}$ is the thermal diffusion coefficient (kg/ms).

The mass diffusion coefficient, $D_{i,m}$, is determined from the binary mass diffusivity (m^2/s), D_{ij}, which governs the diffusion between any two species i

and j. The binary mass diffusivity, D_{ij}, is calculated using Chapman-Enskog theory [28] as,

$$D_{i,m} = \frac{1 - X_i}{\sum\limits_{j \neq i} \left(\frac{X_j}{D_{ij}} \right)} \,.$$

(7)

The thermal diffusion coefficient is defined using an empirically-based composition dependent expression [29] as,

$$D_{T,i} = -2.59 \cdot 10^{-7} T^{0.659} \left[\frac{M_{w,i}^{0.511} X_i}{\sum\limits_{i=1}^{n} M_{w,i}^{0.511} X_i} - Y_i \right] \left[\frac{\sum\limits_{i=1}^{n} M_{w,i}^{0.511} X_i}{\sum\limits_{i=1}^{n} M_{w,i}^{0.489} X_i} \right].$$

(8)

A short reaction scheme (25 species, 121 reactions) is employed to model reactive flow. This mechanism is obtained after eliminating all hydrocarbon species higher than C_2 and nitrogen containing species except N_2 along with their associated reactions from the GRI 2.11 mechanism (a chemical kinetics mechanism used for simulating reactive flows of natural gas–methane) [30]. The total entropy generated per unit volume of a multicomponent, reacting mixture can be divided into five terms [31]. They are, entropy generation due to heat transfer (S_h), mass transfer (S_m), coupling between heat and mass transfer (S_c), chemical reactions (S_r) and viscous dissipation term (S_v). The total rate of entropy generation (S_t) of the system is given as (in W/(m^3 K)),

$$S_t = S_h + S_m + S_c + S_r + S_v \,.$$

(9)

Assuming that the rate of entropy generation due to viscous dissipation (S_v) is negligible, the rates of entropy generated per unit volume for each term in the right hand side of Eq. (9) are calculated as follows:

Entropy generated per unit volume due to heat transfer is calculated as,

$$S_h = \frac{k(\nabla T)^2}{T^2} \,.$$

(10)

Entropy generated per unit volume due to mass transfer is expressed as,

$$S_m = \frac{-\rho R_u}{\bar{W}} \sum_i v_i \cdot \nabla X_i \,.$$

(11)

Here, the ordinary mass diffusion velocity (v_i, m/s) is given as,

$$v_i = \frac{-D_{i,m}}{Y_i} \nabla Y_i \,,$$

(12)

which satisfies the constraint,

$$\sum_i Y_i v_i = 0.$$

(13)

Entropy generated per unit volume due to coupling between heat and mass transfer is evaluated as,

$$S_m = \frac{-\rho R_u}{\bar{W}T} \sum_i w_i \cdot \nabla X_i . \tag{14}$$

Here, the thermal diffusion velocity (w_i, m/s) is given by,

$$w_i = \frac{-D_{T,i}}{\rho Y_i} \frac{\nabla T}{T} \tag{15}$$

subjected to the constraint,

$$\sum_i Y_i w_i = 0. \tag{16}$$

Entropy generated per unit volume due to chemical reactions is given as,

$$S_r = \frac{-1}{T} \sum_i \mu_{c,i} \dot{\omega}_i''' . \tag{17}$$

Here, $\mu_{c,i}$ is the chemical potential calculated as $\mu_{c,i} = h_i - Ts_i$.

2.1. Computational domain

The coflow burner reported in Mokhov et al. [32] has been considered for the present study. The burner is made up of a stainless-steel tube with an inner diameter of 7 mm and a wall thickness of 1.5 mm. The coflow tube has an inner diameter of 95 mm. Fig. 1 shows a schematic of the two-dimensional axisymmetric computational domain along with boundary conditions.

2.2. Boundary conditions

With respect to Fig. 1, the various conditions imparted at the boundaries of the computational domain are listed as follows:

1. **Fuel inlet:** At this boundary fuel mixture enters the domain with a specified velocity and a given temperature (varied between 300 K to 700 K) and atmospheric pressure. Appropriate mass fractions of the fuel components (CH_4, CO_2 and H_2, if used) are also specified.

2. **Coflow air inlet:** Air is supplied at a uniform velocity at a given temperature (varied between 300 K to 700 K) at atmospheric pressure through this boundary. The mass fractions of O_2, N_2 and H_2 (if used) are also specified.

3. **Pressure outlet:** Pressure is specified at this boundary. The flow direction is determined based on its gradient. In the case of a favourable pressure gradient, the flow variables are extrapolated from the neighbouring interior cells within the domain. The first spatial derivative of all the flow variables are set to zero
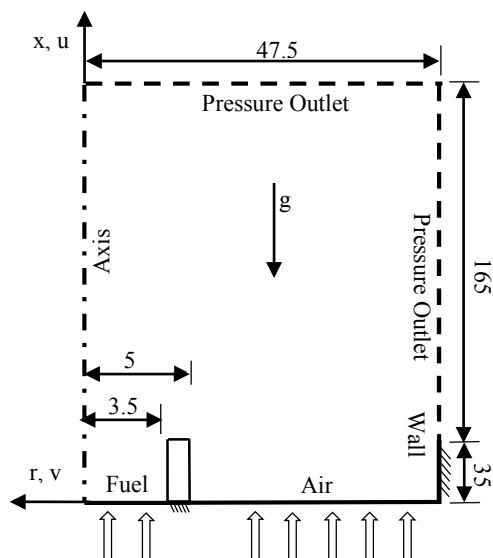
Fig. 1. Schematic of computational domain (all dimensions in mm)

at this boundary. If a reverse flow occurs due to adverse pressure gradient, atmospheric air (0.233 O_2 by mass, rest nitrogen) at a temperature of 300 K enters through this boundary.

4. **Walls:** All the walls at the domain boundary are specified with a constant temperature of 300 K. No slip condition ($u = v = 0$) is specified for velocity. First-order derivatives of species mass fractions (normal to boundary) are set to zero. All the wall surfaces in contact with the fluid region are solved for heat transfer in a coupled manner within the computational domain.

5. **Axis:** The radial velocity, v, and the radial gradients of all variables such as flow, species and temperature are set to zero.

The convergence criteria have been set as normalized residual values below 10^{-6} for continuity, momentum, species and energy conservation equations. Further, the mass imbalance is kept within 1% relative to the least incoming flow into the domain.

2.3. Grid independence study

Three non-uniform, structured grids with 16 245, 32 775 and 56 350 cells have been considered for grid independence study. Temperature profiles predicted using these grids are compared (Fig. 2). The results do not change notably when the number of cells is increased from 32 775 to 56 530. Therefore, a grid with 32 775 cells, having a minimum cell size of 0.25 mm in the radial and 0.5 mm in the axial direction has been chosen for parametric study.

(a) 9 mm

(b) 14 mm

(c) 19 mm

(d) 24 mm

(e) 29 mm
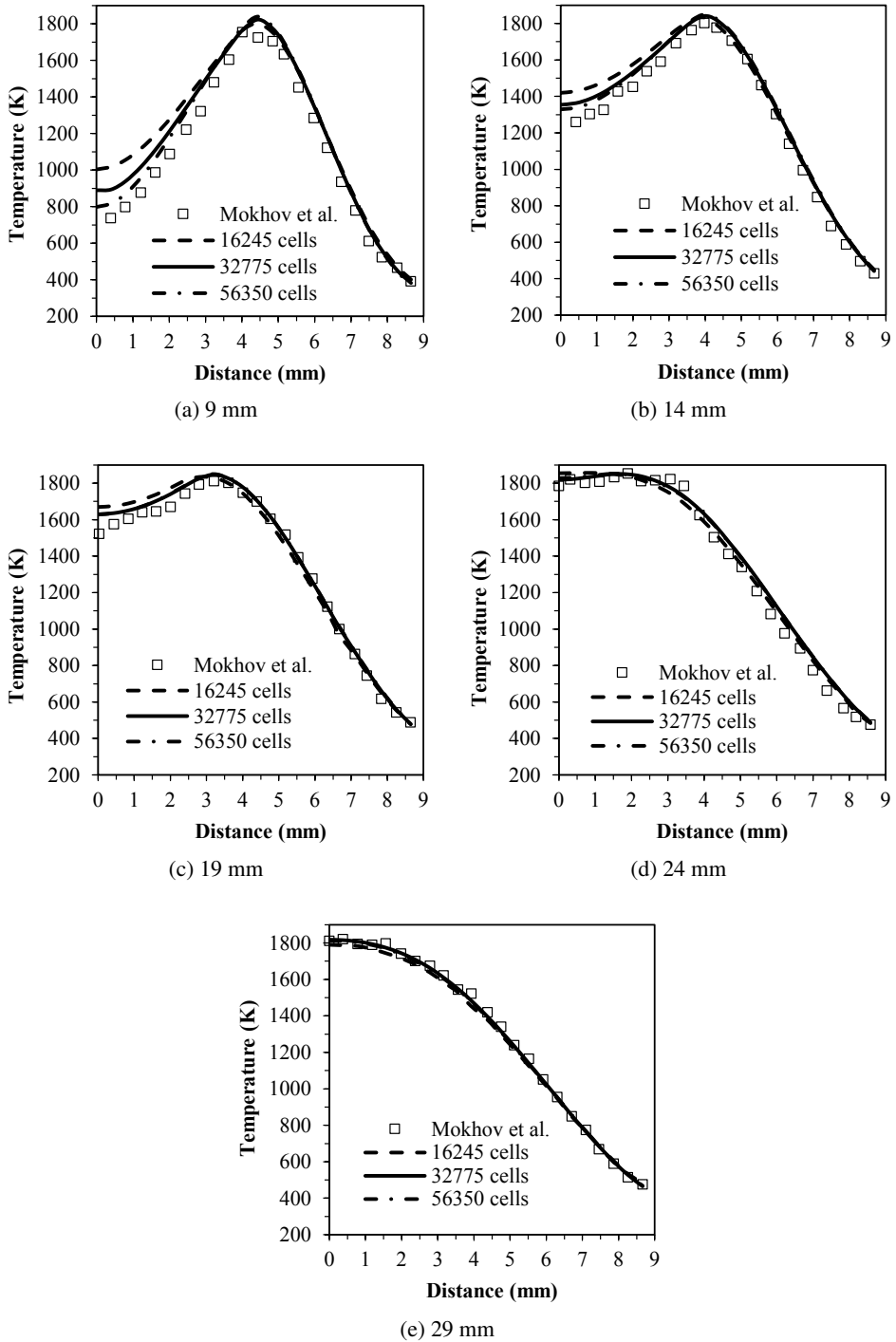
Fig. 2. Radial temperature profile validated against Mokhov et al. [32] at various axial locations

2.4. Validation

The experimental data for validating biogas coflow diffusion flames are scarce in literature. Therefore, the numerical results are validated using the experimental data reported in Mokhov et al. [32] for methane coflow diffusion flames diluted with nitrogen. Methane (40% by volume) diluted with N_2 (60%) is used in the fuel stream. Velocities of both fuel and coflow air are fixed at 0.13 m/s. It is clear from Fig. 2 that the numerical model is able to predict the measured temperature profiles quite accurately. Additional validation of the numerical model with temperature and species concentration profiles in methane-air opposed flow flames reported in Sung et al. [35] is shown in Appendix A.

3. Results and discussion

3.1. Parametric study

The power rating of the burner is kept as 0.25 kW for all cases. A parametric study is carried out by varying the amount of CO_2 in biogas as 30%, 37.5% and 45% by volume to understand the effects of CO_2 content in the fuel on flame characteristics. The case with maximum amount of CO_2 in the fuel is used as the baseline case. The effects of preheated fuel or air on the flame stability and characteristics are analysed for this baseline case. The maximum temperature of the fuel or the air stream for the cases with preheated reactant has been limited to 700 K. The energy required for preheating the fuel or air to the maximum temperature of 700 K corresponds to 2.5% (preheating fuel) or 15% (preheating air) of the burner power. The mass flow rate of air in these cases is kept at stoichiometric value. The cases are listed in Table 1.

Table 1. List of cases with varying CO_2, fuel and air stream temperature

Case No	Air temperature (K)	Fuel temperature (K)	CH_4 (mole %)	CO_2 (mole %)	Mass flow rate of fuel (kg/s)	Mass flow rate of air (kg/s)
			Effect of CO_2			
1	300	300	70	30	1.072×10^{-5}	8.49×10^{-5}
2	300	300	62.5	37.5	1.304×10^{-5}	8.49×10^{-5}
3	300	300	55	45	1.598×10^{-5}	8.49×10^{-5}
			Effect of preheated air			
4, 5, 6, 7	400, 500, 600, 700	300	55	45	1.598×10^{-5}	8.49×10^{-5}
			Effect of preheated fuel			
8, 9, 10, 11	300	400, 500, 600, 700	55	45	1.598×10^{-5}	8.49×10^{-5}

The flame stability and characteristics of the baseline case is studied by adding varying amounts (by volume, keeping the same mass) of hydrogen to the fuel and air streams separately. The mass flow rate of hydrogen is chosen such that the percentage of energy contributed by hydrogen to the total energy of the fuel mixture is not more than 10% in any case. Table 2 presents the list of these cases.

Table 2. List of cases with varying hydrogen in the fuel and air streams (Biogas composition: $CH_4 - CO_2$: 55 – 45 and energy added by biogas = 0.25 kW)

Case No	H_2 (% by volume)		H_2 mass flow rate (kg/s) $\times 10^{-8}$		Energy added by hydrogen (kW)	Energy added by hydrogen (%)	Total mass flow rate (kg/s) $\times 10^{-5}$	
	Fuel	Air	Fuel	Air			Fuel	Air
12	5	–	5.83	–	0.007	2.72	1.60	8.49
13	10	–	12.3	–	0.015	5.62	1.61	8.49
14	15	–	19.5	–	0.024	8.55	1.618	8.49
15	–	1	–	5.83	0.007	2.72	1.598	8.495
16	–	2	–	12.3	0.015	5.62	1.598	8.502
17	–	3	–	19.5	0.024	8.55	1.598	8.509

3.2. Effects of CO_2 fraction

When the amount of CO_2 in biogas is varied as 30%, 37.5% and 45% by volume, Fig. 3 presents the isolines of temperature along with mass fraction of CH_4. The maximum flame temperature is 1884 K for Case 1 (30% CO_2). It is observed that the maximum temperature continuously decreases with an increase in the amount of CO_2 in the fuel mixture because of higher specific heat and radiation absorption nature of CO_2. The forward rate of the main exothermic reaction, $CO + OH \leftrightarrow CO_2 + H$, also decreases with an increase in CO_2 content [5], which further reduces the heat release rate. Since CO_2 is non-combustible, to contribute to the fixed power rating of 0.25 kW, a higher flow rate for the fuel mixture is required when it contains higher fraction of CO_2. Therefore, the flow residence time decreases with increasing CO_2 fraction. As a result, the flame starts to move away from the burner rim and anchors at a certain distance, where reaction and flow times are in equilibrium. This is indicated by the isotherms of 500 K and 1000 K. The radial extent of the maximum flame zone (reaction zone) remains almost unaffected (only a slight decrease is seen). Stoichiometric fuel-oxygen ratio ($\Phi = 1$) is calculated as $Y_{fuel} - Y_{oxygen}/\nu = 0$. Isoline of $\Phi = 1$ (dashed line in Fig. 3) is embedded within the high temperature zone in all the cases. It is noted that, near the burner rim, the stoichiometric contour line moves radially inwards indicating good mixing of methane and oxygen; however, due to the higher flow rate, the flame lifts-off as the CO_2 fraction is increased. The gradient of methane concentration decreases with increasing CO_2 fraction.
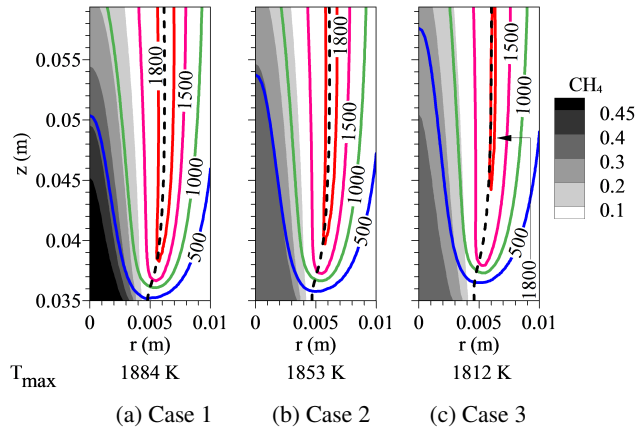
Fig. 3. Contours of temperature (lines) with methane mass fraction (greyscale)
for different cases. Dashed line indicates stoichiometric contour line ($\Phi = 1$)

Fig. 4 shows the contours of oxygen and H mass fractions along with mixture velocity vectors. The O_2 mass fraction contour of 0.02 is embedded within the core reaction zone (Fig. 3), showing its consumption zone. The curvature in isoline of 0.08 indicates the flame anchoring position near the burner rim. The velocity vectors depict the flow acceleration and air entrainment towards the flame zone. In Cases 2 and 3 with higher CO_2, a higher fuel velocity prevails. Air entrainment also increases and as a result, the mixing of reactants is enhanced. Reduction in the residence time for the reactants to burn, causes flame lift-off and the flame sustains as a partially premixed lifted flame. But, for the presence of higher amount of CO_2, the flame temperature would have been the same or slightly higher. The intensity in the mass fraction of H, the main radical for chain initiation and propagating reactions, decreases as CO_2 in the fuel is increased. Its maximum value for Cases 1, 2 and 3, are 5.7e-05, 4.6e-05 and 4.0e-05, respectively.
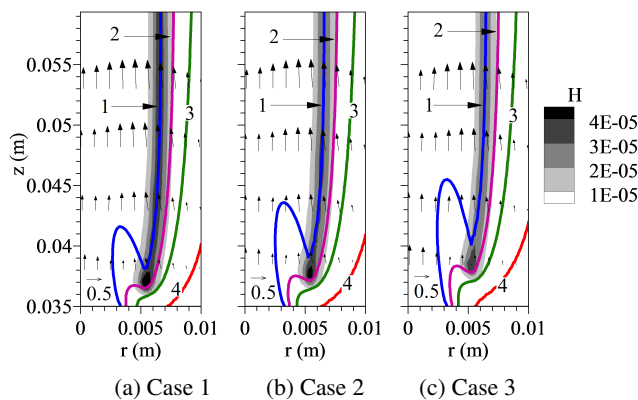
Fig. 4. Contours of O_2 (lines) and H (greyscale) mass fractions, along with velocity
vectors for different cases. [Label O_2: 1 – 0.02, 2 – 0.08, 3 – 0.16, 4 – 0.23]

Fig. 5 depicts the contours of OH (lines) and CO (greyscale) mass fractions for Cases 1 to 3. The maximum values of CO are 0.033, 0.032 and 0.03, for Case 1, Case 2 and Case 3, respectively, displaying only a slightly decreasing trend. Corresponding maximum values of OH, 0.00216, 0.002 and 0.00178, decrease with an increase in CO_2. With an increase in CO_2 content in the fuel mixture, the rate of the forward reaction in the reversible elementary reaction, $CO + OH \leftrightarrow CO_2 + H$, decreases, reducing the production of CO_2 from CO [5]. Since H is in the product side, the production of radical H will also decrease eventually. This could cause a reduction in OH. Further, due to a decrease in the concentration of methane, which is the primary source of CO and OH, the concentrations of CO and OH decrease with an increase in CO_2 content. The inner contour line of minimum OH mass fraction intersects with the maximum temperature contour (Fig. [3]) in all these cases. The CO consumption zone occurs around the outer contour line of minimum OH mass fraction.
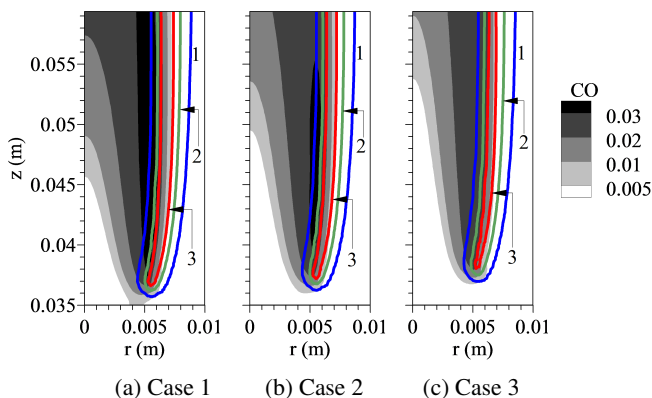
Fig. 5. Contours of CO (greyscale) and OH (lines) mass fractions for different cases. [Label: OH: 1 – 0.0001, 2 – 0.0007, 3 – 0.0015]

3.3. Effect of preheated fuel and air

The stability of diffusion flame can be improved by preheating the fuel or air streams or both [33, 34]. In this section, the effect of preheating the air or the fuel stream on flame stability is reported. The temperature of the fuel stream or the coflow air stream is varied from 300 K to 700 K in the interval of 100 K. These cases are shown as Cases 4 to 7 for preheated air and Cases 8 to 11 for preheated fuel (Table 1).

Fig. 6 shows the comparison of temperature contours for the cases with preheated fuel (left side) keeping air temperature at 300 K and the cases with preheated coflow air (right side), keeping fuel temperature at 300 K. For preheated fuel, the maximum flame temperature marginally increases from 1812 K (Case 3) to 1832 K (Case 11) with a corresponding increase in fuel temperature from 300 K to 700 K.

An increase in fuel temperature results in flame movement closer to the burner rim, indicating an increase in the flame stability.
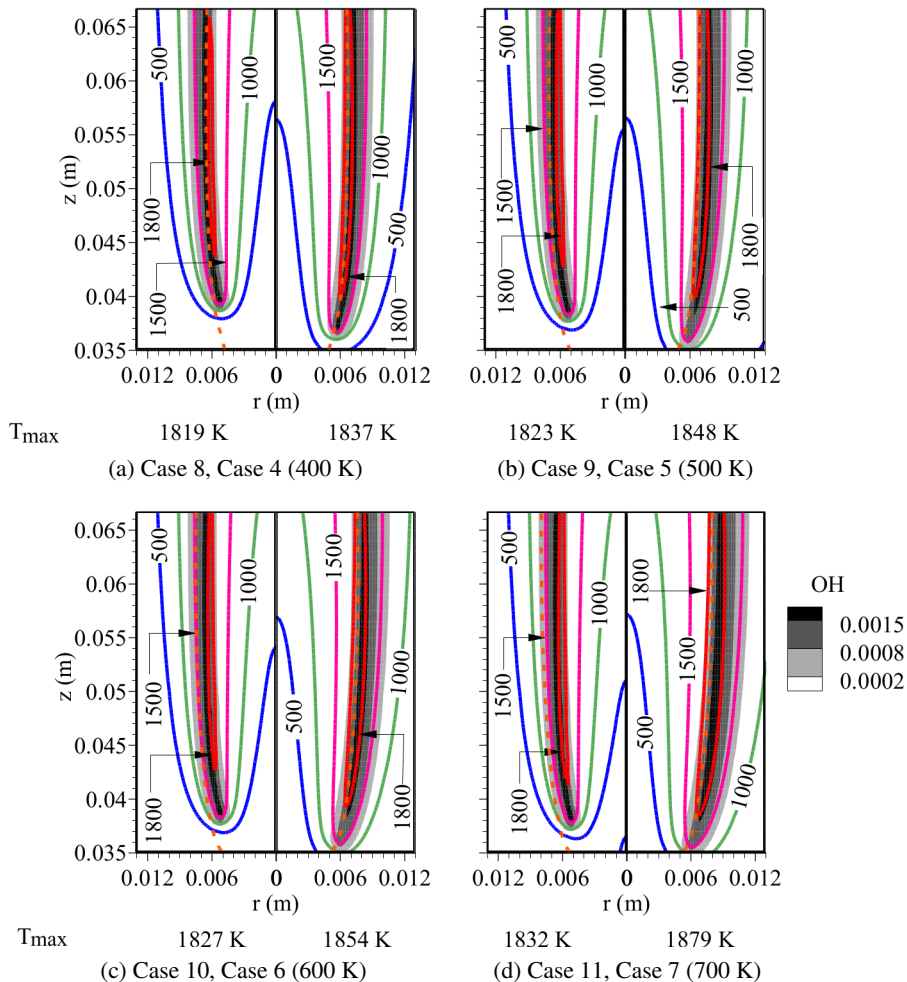

Fig. 6. Contours of temperature (lines) with OH mass fraction (greyscale) in cases with preheated fuel (left) and air (right) for different cases. Dashed line indicates stoichiometric contour line ($\Phi = 1$)

On the other hand, with preheated air, the flame becomes more stable at a lower preheat temperature of 400 K itself. This is because of the higher energy supplied for preheating the air to that temperature, when compared to the energy required for preheating the fuel. Due to preheated reactants, the heat release (standard heat of combustion cooling the products to 298 K) also increases. The ratio of heat required to preheat the fuel to the standard heat of combustion (products cooled to 298 K), varies in the range of 0.5% to 2.3% for 300 K to 700 K, respectively. The same ratio for air stream varies in the range of 0.2% to 0.75% for 300 K to 700 K. The average heat flow rate from domain exit for the baseline case is around

178 W and the heat required to increase the temperatures of fuel and air streams to 700 K are 10.4 W and 34 W, respectively. The width of the flame, following the isotherm of 500 K or 1000 K, increases with an increasing air preheat temperature. The radial movement of the flame away from the axis is also clearly indicated by the stoichiometric contour line. This is due to an increase in the rate of diffusion at higher reactant temperatures. As seen earlier, the stoichiometric contour lines almost intersect with the high temperature zone irrespective of preheating fuel or air. Maximum OH mass fraction lies just radially outside of the stoichiometric contour line.

Fig. 7 shows the comparison of oxygen mass fraction contours along with mixture velocity vectors for cases with preheated fuel and coflow air. The isoline

(a) Case 8, Case 4 (400 K) (b) Case 9, Case 5 (500 K)

(c) Case 10, Case 6 (600 K) (d) Case 11, Case 7 (700 K)
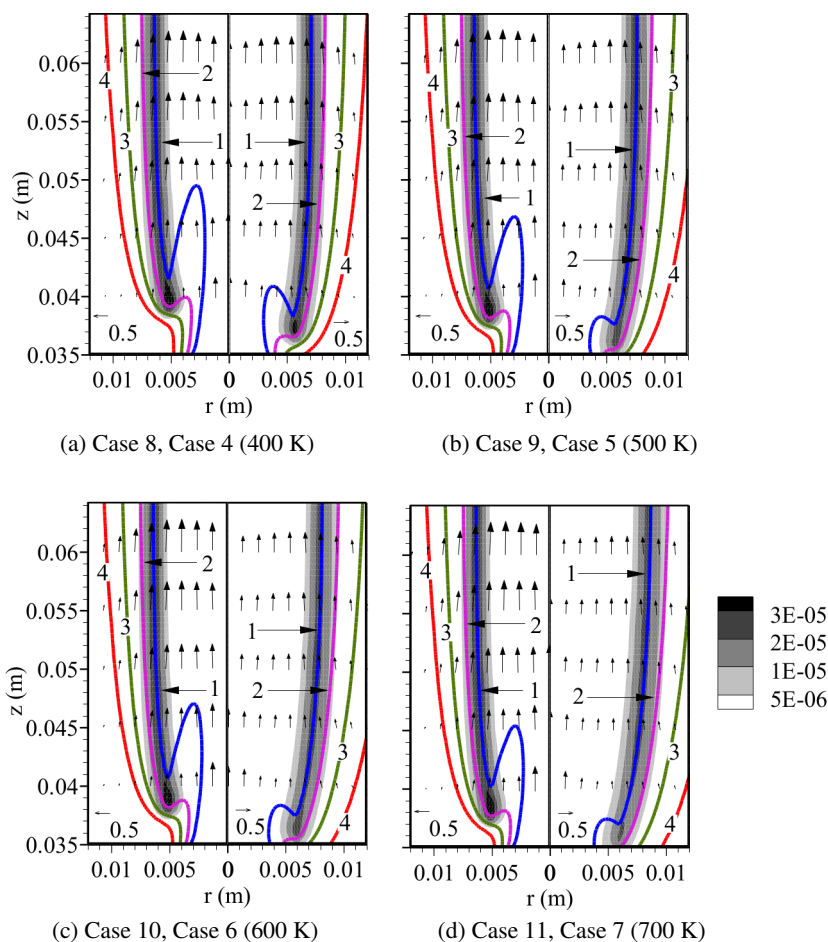
Fig. 7. Contours of O_2 (lines) and H (greyscale) mass fractions, along with velocity vectors in cases with preheated fuel (left) and air (right) for different cases.
[Label: O_2: $1 - 0.02$, $2 - 0.08$, $3 - 0.16$, $4 - 0.21$]

of O_2 mass fraction 0.02 lies inside the core reaction zone (Fig. 6). Oxygen mass fraction line of 0.08 bounds the mass fraction of H on the air side of the flame and its curvature towards the flame base indicates the flame anchoring region for all the cases. With preheated fuel, the flame radius remains almost the same across the cases.

However, in preheated air cases, the flame radius is higher and it increases with the degree of preheat. The curvature in the contour line of O_2 mass fraction of 0.08 moves close to the burner rim with increase in temperature of fuel stream whereas it decreases gradually and finally disappears for Case 7 (700 K) indicating an improved flame stability at higher air temperature, where more preheat energy has come in relative to the preheated fuel at the same temperature. The velocity vectors clearly show the plume acceleration in the flame zone for all the cases as expected.

3.4. Effect of H_2 addition

Subsequently, the effect of adding hydrogen to the fuel or coflow air stream is analysed. Biogas with maximum CO_2 in the fuel mixture (Case 3) is chosen as the baseline. A specified mass flow rate of hydrogen is added only to the fuel stream (Case 12, Case 13 and Case 14). Similarly, the specified mass flow rate is added only to the air stream (Case 15, Case 16 and Case 17). These cases are shown along with energy contributed by H_2 in Table 2. Power share of biogas is kept constant at 0.25 kW (in order to keep the CO_2 content in the fuel the same) and the maximum energy contributed by hydrogen is kept as 8.55%.

Fig. 8 presents the temperature field (lines) along with OH mass fraction (greyscale) contours for the cases with varying amount of H_2 in the fuel and air stream. The maximum temperature increases from 1812 K (baseline case) to 1849 K (15% H_2 by volume in fuel stream) and 1851 K (3% H_2 by volume in the air stream).

The high temperature zone descends towards the burner rim with increasing H_2 concentration in the fuel or air stream. The flame begins to anchor near to the burner rim when the hydrogen content is 10% by volume in the fuel stream (Case 13 in Fig. 8c) and 2% in the air stream (Case 16 in Fig. 8f). The flame width, indicated by the isotherm 1000 K, increases with an increasing H_2 concentration, especially in the air side, due to the increase in the thickness of the preheat zone caused by the oxidation of hydrogen in the mixture. The slight outwards radial movement of the flame zone is clearly shown by the stoichiometric contour line, which coincides with the maximum temperature location. Due to high diffusivity and reactivity of hydrogen, the oxidation of fuel occurs immediately near the burner rim. With an increase in the H_2 concentration in the fuel or air stream, the production of OH increases, which further enhances the oxidation of CO and hence the flame temperature.
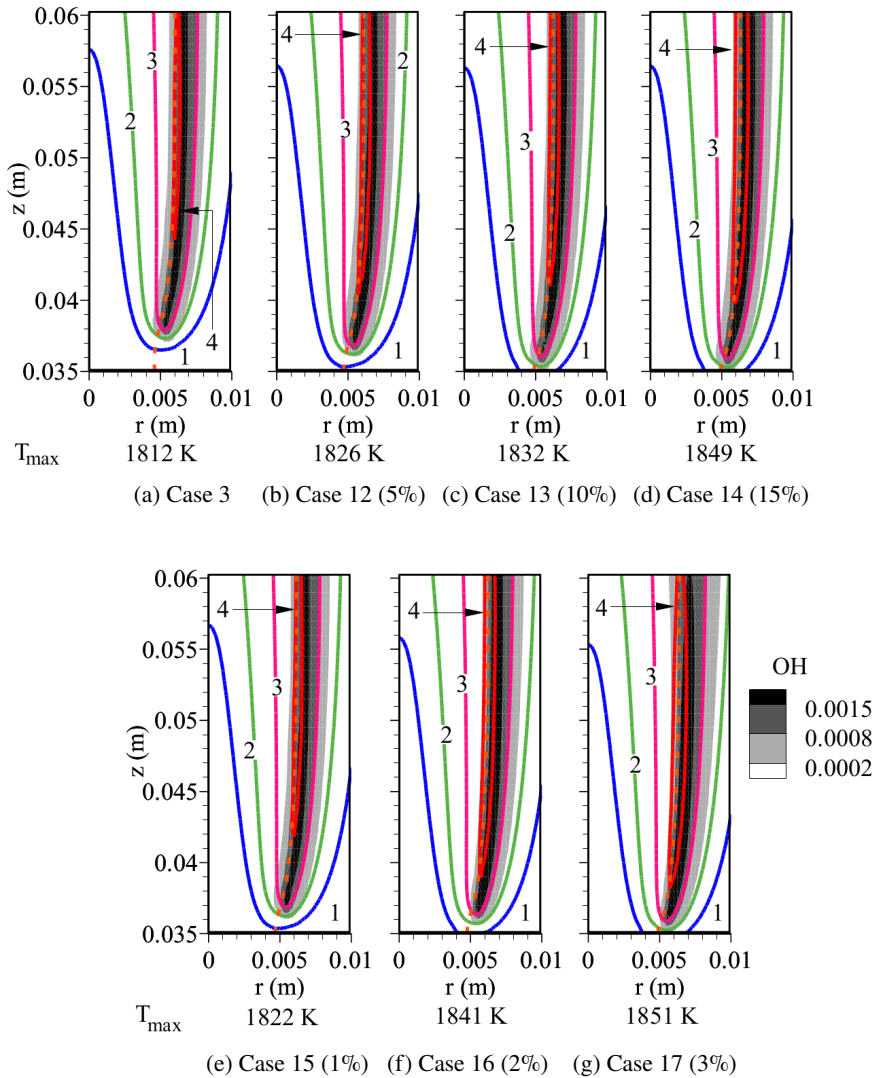
Fig. 8. Contours of temperature (lines) with mass fraction of methane (greyscale) for different cases.
Dashed line indicates stoichiometric contour line ($\Phi = 1$).
[Label: Temperature (K): 1 – 500, 2 – 1000, 3 – 1500, 4 – 1800]

Fig. 9 presents the fields of oxygen and H, along with mixture velocity vectors for the Cases 3, 12 to 17. Penetration of O_2 towards the fuel side is shown by the isoline of 0.02, which lies close to the maximum temperature. The contour line of O_2 mass fraction of 0.08 indicates the flame anchoring location by its curvature, as seen before. There is a slight increase in the flow velocity due to addition of hydrogen in the fuel stream. The velocity vectors show the oxygen entrainment in the flame zone due to high momentum of the fuel jet and flow acceleration in

the plume region due to buoyancy effects. The intensity of the H field is seen to increase with H_2 addition and is more pronounced when hydrogen is added to the fuel stream.
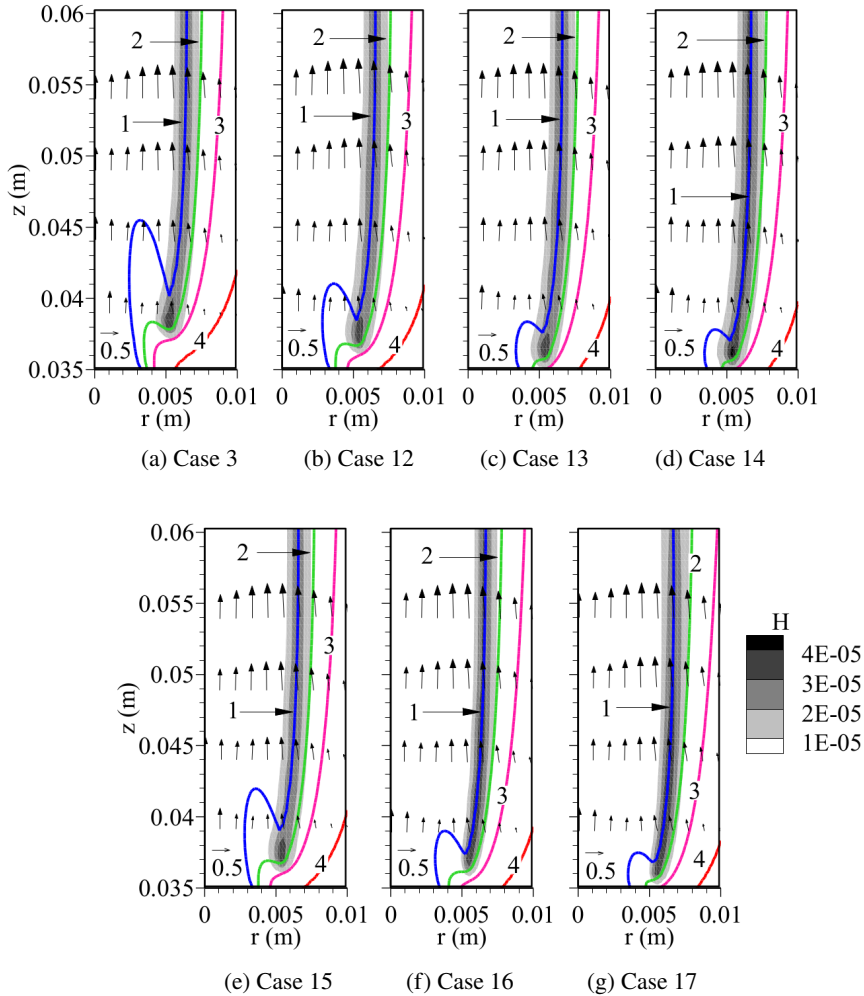
Fig. 9. Contours of O_2 (lines) and H (greyscale) mass fractions, along with velocity vectors for different cases.
[Label O_2: $1 - 0.02$, $2 - 0.08$, $3 - 0.16$, $4 - 0.23$]

3.5. Entropy generation

Fig. 10 shows the contours of entropy generation rate per unit volume for Case 1 with 30% CO_2 content in biogas. Volume integrated values are shown within the plots. Entropy generation due to heat transfer is higher near the burner rim on

both preheat zones and the maximum value is found on the air side. The entropy generation due to chemical reactions occurs in the flame zone and contributes majorly to the total entropy generation. Maximum entropy generation due to mass transfer also occurs near the burner rim, where fresh oxygen diffuses into the fuel. Entropy generated due to coupled heat and mass transfer is the least among all others.
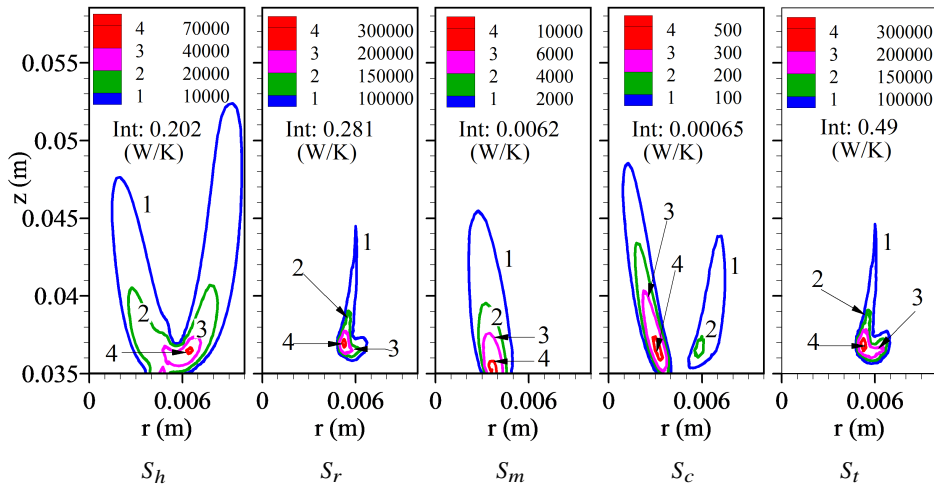
Fig. 10. Contours of entropy generation rate per unit volume (W/m^{3}K) due to heat transfer (S_h), reaction (S_r), mass transfer (S_m), coupled heat and mass transfer (S_c) and total entropy (S_t) for Case 1 (30% CO_2 content in biogas). Integrated values (W/K) are shown in plots

Fig. 11 presents the entropy generation per unit volume for cases with preheated air at 400 K and 700 K. Maximum entropy generated due to heat transfer increases with an increase in the temperature of preheated air, however, the integrated value decreases.

The branch towards the fuel side is only visible with an increase in preheat air temperatures, as the flame has moved towards the burner rim at 700 K. However, the maximum entropy generated due to chemical reactions and the integrated value decrease with an increase in air temperature. The movement of maximum valued contour towards the burner rim at 700 K shows improved flame stability. The entropy generated due to mass transfer marginally increases and that due to coupled heat and mass transfer marginally decreases with an increase in air temperature. The axial extent of the field of entropy generated due to mass transfer increases with an increase in air temperature. The contours of total entropy generated follows that due to chemical reactions and its integrated value decreases with an increase in air temperature. This indicates that the overall irreversibility decreases with air preheating.
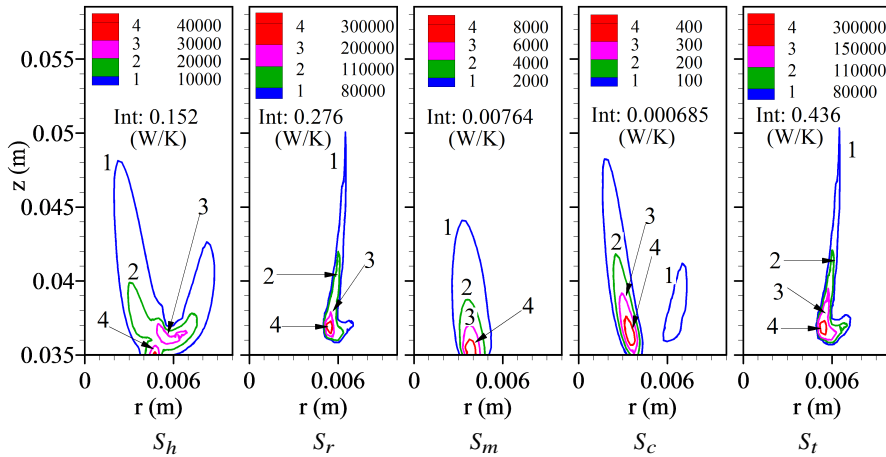
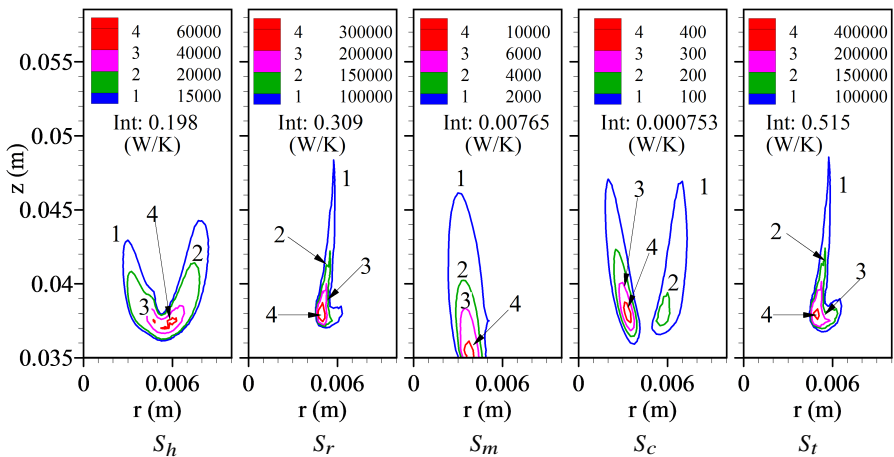(a) Case 4 with preheated air at 400 K
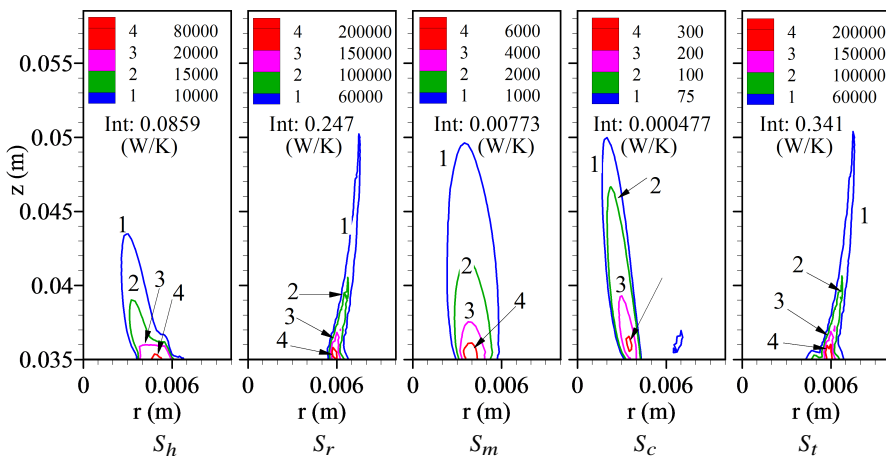
(b) Case 7 with preheated air at 700 K

Fig. 11. Contours of entropy generation rate per unit volume (W/m^{3}K) due to heat transfer (S_h), reaction (S_r), mass transfer (S_m), coupled heat and mass transfer (S_c) and total entropy (S_t) for different cases. Integrated values (W/K) are shown in plots

Fig. 12 shows the entropy generation per unit volume for cases with preheated fuel at 400 K and 700 K. Patterns and trends remain almost the same between these two cases. The entropy generated due to heat transfer and that due to chemical reactions marginally increase with an increase in preheated fuel temperature, resulting in a marginal rise in the total entropy generation. The entropy generated due to mass transfer and that due to coupled heat and mass transfer processes remain almost the same. The contours move close to the burner rim with an increase in fuel temperature, showing an increase in the stability. As compared to air preheated cases, irreversibility marginally increases with fuel preheating.
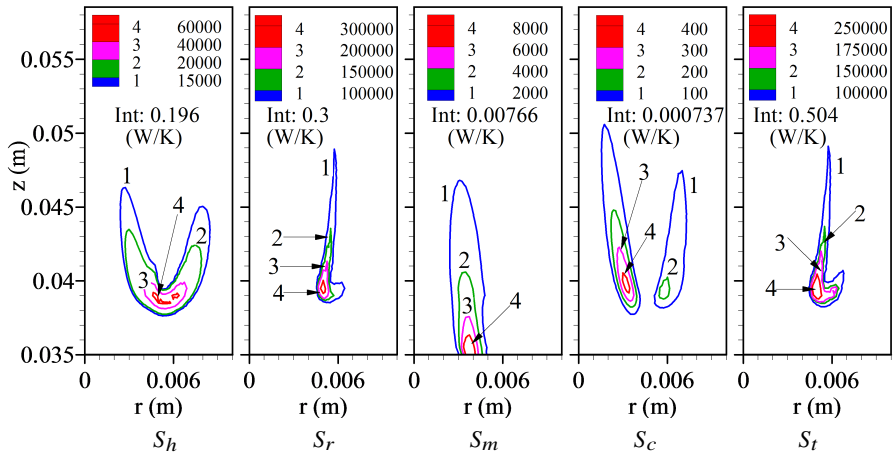
(a) Case 8 with preheated fuel at 400 K

(b) Case 11 with preheated fuel at 700 K

Fig. 12. Contours of entropy generation rate per unit volume (W/m^{3}K) due to heat transfer (S_h), reaction (S_r), mass transfer (S_m), coupled heat and mass transfer (S_c) and total entropy (S_t) for different cases. Integrated values (W/K) are shown in plots

Fig. 13 depicts the contours of entropy generation per unit volume for cases with 5% and 15% hydrogen added to the fuel stream. The contours shift closer to the burner rim with an increase in H$_2$ addition indicating increasing stability. An increasing trend in entropy generation in all processes is observed with increasing H$_2$ content. Axial extents of S$_m$ and S$_c$ increase with increasing H$_2$ due to the higher diffusion rate. Other trends and patterns remain almost the same. It can be concluded that increased flame stability is got at an expense of marginal increase in irreversibility, when H$_2$ is added to the fuel stream.
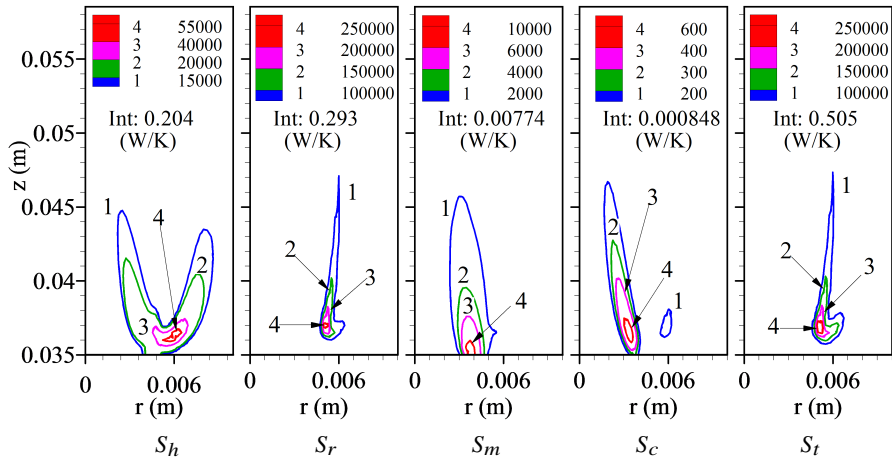
(a) Case 12 with 5% H_2 in fuel stream
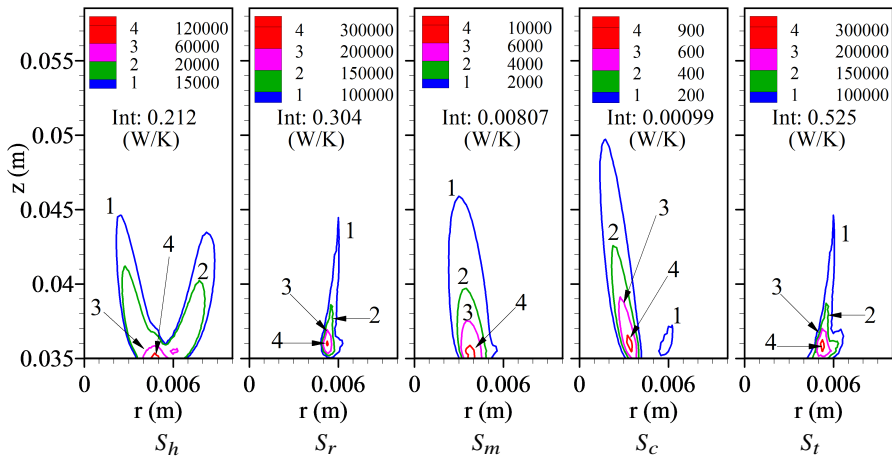
(b) Case 14 with 15% H_2 in fuel stream

Fig. 13. Contours of entropy generation rate per unit volume (W/m^{3}K) due to heat transfer (S_h), reaction (S_r), mass transfer (S_m), coupled heat and mass transfer (S_c) and total entropy (S_t) for different cases. Integrated values (W/K) are shown in plots

Fig. 14 presents the entropy generation per unit volume for the cases with 1% and 3% H_2 added to the air stream. Notable differences in the extents of the contours are seen between the two cases. Marginal increase in S$_h$, S$_r$ and S$_t$ values is observed with increased H_2 in air stream. On the other hand, a decrease in the values of S$_m$ and S$_c$ is observed with increasing H_2 in air stream. The contours shift towards the burner rim and their extents reduce as a result of increased H_2 in air stream. For the similar energy contribution by H_2, whether it is added to fuel or air streams, the resultant marginal increase in irreversibility is observed to be almost the same. An increased stability is seen in both the cases.
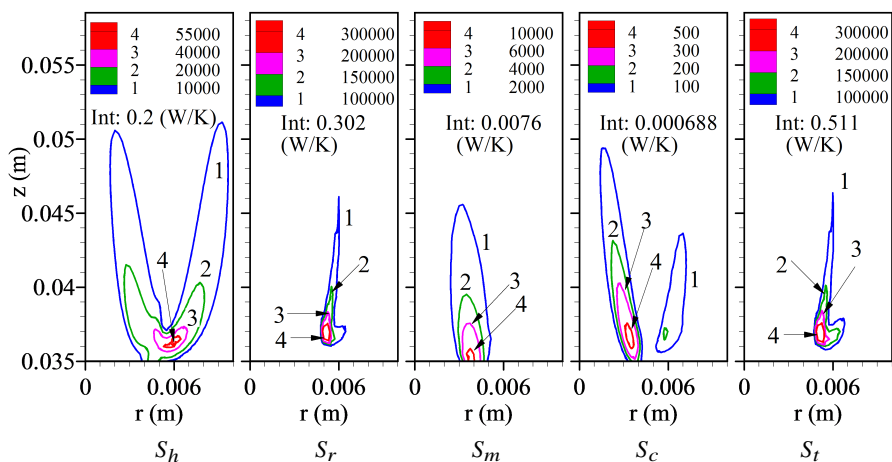
(a) Case 15 with 1% H_2 in air stream
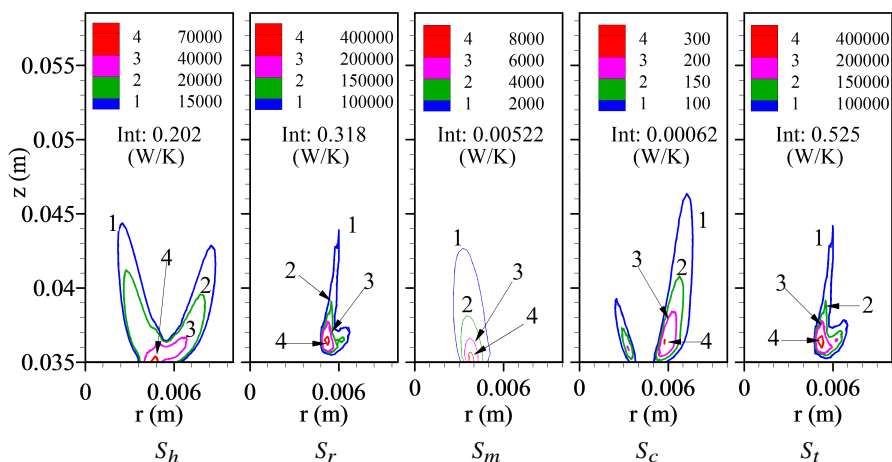
(b) Case 17 with 3% H_2 in air stream

Fig. 14. Contours of entropy generation rate per unit volume (W/m^{3}K) due to heat transfer (S_h), reaction (S_r), mass transfer (S_m), coupled heat and mass transfer (S_c) and total entropy (S_t) for different cases. Integrated values (W/K) are shown in plots

Fig. 15 presents the volume integrated entropy generation (W/K) values for all the cases. It is observed that total entropy generated follows the trend of entropy generated due to chemical reaction in most of the cases and in a few both S_h and S_r together contribute to S_t. The entropy generated due to heat transfer and chemical reactions contribute to around 98% of the total entropy generation. In all these, as discussed earlier, contributions of S_m and S_c are quite small.

Fig. 15a presents the volume integrated entropy generation in cases 1, 2 and 3 with varying CO_2 in biogas. Irreversibility due to chemical reactions is observed
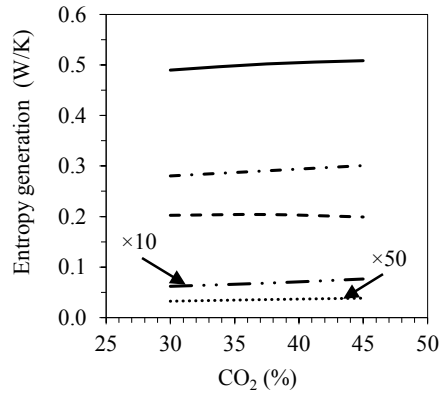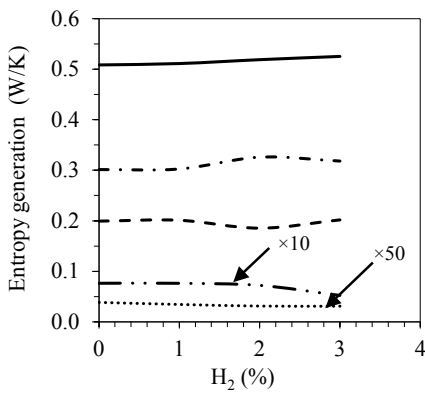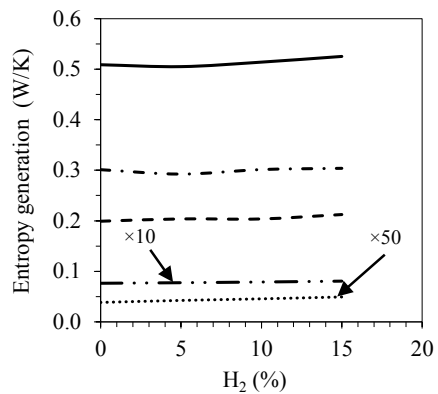
(a) CO_2 in biogas
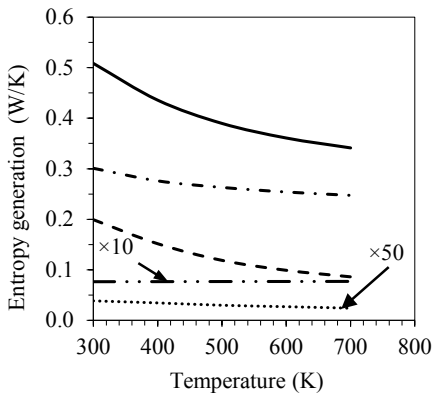
(b) preheat air temperature
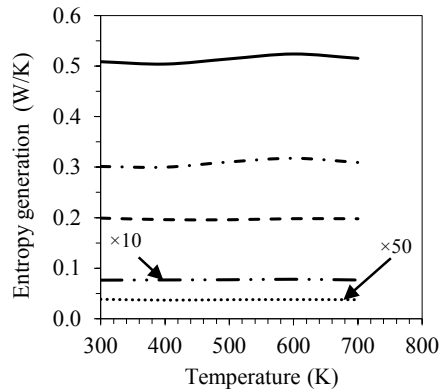
(c) preheat fuel temperature

(d) H_2 addition to air stream

(e) H_2 addition to fuel stream

Fig. 15. Entropy generation rate (W/K) as a function of various factors
$- - - S_h \quad - \cdot \cdot - S_m \quad \cdots \cdot S_c \quad - \cdot - \cdot S_r \quad \text{——} S_t$

to slightly increase with CO_2 content in the fuel mixture. The value of S_h shows a slight decreasing trend due to reduction in the flame temperature with increasing CO_2 content. As a result, the total irreversibility increases only marginally (by around 3.85%) between the three cases. However, flame stability is affected with increasing CO_2 content, as discussed earlier in the flame structure (Figs. 3–5).

For the cases with preheated air (Fig. 15b), significant drop (around 33%) in the value of total entropy generation is observed as air temperature is increased from 300 K to 700 K. It should be noted that this has been an effective way to increase the flame stability as demonstrated in Figs. 6 and 7. Though S_r and S_h present decreasing trends with increasing air temperature, the slope of S_h is relatively steeper, and S_t follows that trend. For the cases with preheated fuel stream (Fig. 15c), even though a local maximum is observed in the variation of S_t and S_r, their overall variation is within 3.5%. The value of S_h remains almost a constant with varying fuel temperature. It has been shown that preheating fuel stream to higher temperatures (up to 700 K) does not result in an increase in flame stability, as preheated air stream contributes to. Moreover, irreversibility is notably higher in the cases with preheated fuel stream when compared to that with preheated air set to the same temperature.

Figs. 15d and 15e show almost similar trends in S_t for the cases with H_2 addition to air stream (Fig. 15d) and to the fuel stream (Fig. 15e). This indicates that presence of H_2 in either fuel or air stream contributes to similar reaction and preheat zones and similar irreversibility in the reacting flow. Here, the increase in S_t relative to the baseline case of BG45 is only around 3.3%.

However, hydrogen addition, contributing to the same power rating, is seen to be relatively more effective in increasing the flame stability when added to the fuel stream (Figs. 8 and 9). Since in both cases, the total entropy generation is almost the same, to increase the flame stability, hydrogen can be added to the fuel stream.

4. Conclusions

The stability and structure of biogas-air coflow flames are thoroughly analysed using comprehensive numerical simulations done in OpenFOAM with short chemical kinetics mechanism. Flame characteristics and its stability have been studied at different operating conditions. The entropy generation due to various processes such as heat transfer, mass transfer, coupled heat and mass transfer and chemical reactions have been predicted and compared for all the cases. The important conclusions from the present work are: (1) Flame stability is affected by the amount of CO_2 present in biogas, which reduces the flame temperature and the concentrations of H and OH radicals. (2) Preheating the air stream enhances the flame stability in a more pronounced manner when compared to preheating the fuel to the same temperature. However, more energy is required to preheat the air to the same temperature as the fuel stream. The maximum flame temperature

and width of the reaction zone increases with an increase in the temperature of preheated air. (3) The flame stability improves with an addition of hydrogen to the fuel or the air stream. The width of the flame zone increases with addition of hydrogen to the air stream. With an increase in the hydrogen content in the fuel or air stream, the production of OH increases which further enhances the oxidation of CO and hence the flame temperature. The intensity of the H field is seen to increase with H_2 addition and is more pronounced with H_2 addition to the fuel stream. (4) Preheating the air contributes to increased flame stability and also to a significant decrease in entropy generation, when compared to preheating fuel to the same temperature. (5) The presence of hydrogen in either fuel or air stream contributes to similar reaction and preheat zones, causing similar irreversibility in the reacting flow. (6) Hydrogen addition, contributing to the same power rating, is seen to be relatively more effective in increasing the flame stability when added to the fuel stream.

Acknowledgements

A. Appendix A

The numerical model is validated with the temperature and species concentration profiles in methane-air opposed flow flame reported in Sung et al. [35]. The experimental setup has two concentric axisymmetric burners with an inner diameter of 14 mm facing each other and separated by a distance of 13 mm. Methane (23% by mass) diluted with nitrogen is supplied from the bottom burner and oxygen (23%) diluted with nitrogen is supplied from the top burner. The velocity of fuel and air streams are kept as 25.5 cm/s. Nitrogen is supplied through the outer tube on the fuel and air side to prevent the flame from ambient perturbations.

An axisymmetric computational domain with 42 mm in the radial direction and 13 mm in the axial direction is chosen for study. The domain is discretized into uniform cells of size 0.5 mm in the axial and radial directions. Appropriate boundary conditions are set corresponding to the experimental operating conditions. If reverse flow occurs, ambient air with 23.3% O_2 (by mass) and rest nitrogen enters the domain through this boundary. Steady state simulations have been carried out until convergence.

Fig. 16 presents the comparison of predicted flame temperature and species concentration profiles of CH_4, O_2, CO, CO_2 and H_2O with experimental data. It is observed that the model accurately predicts the experimental results.
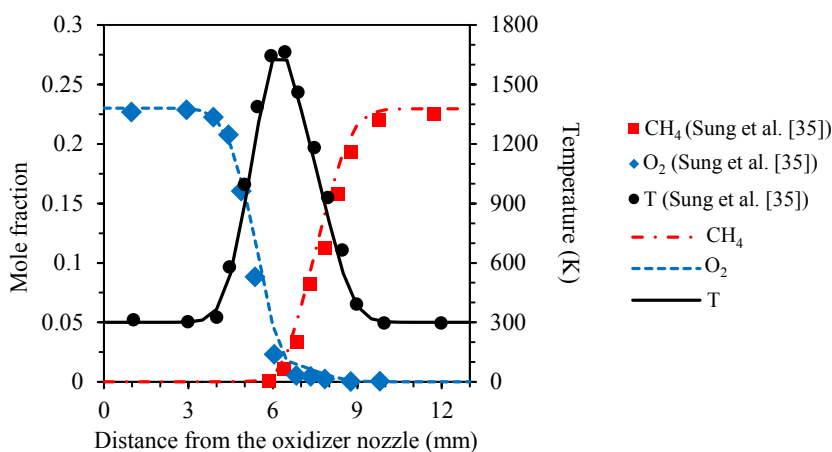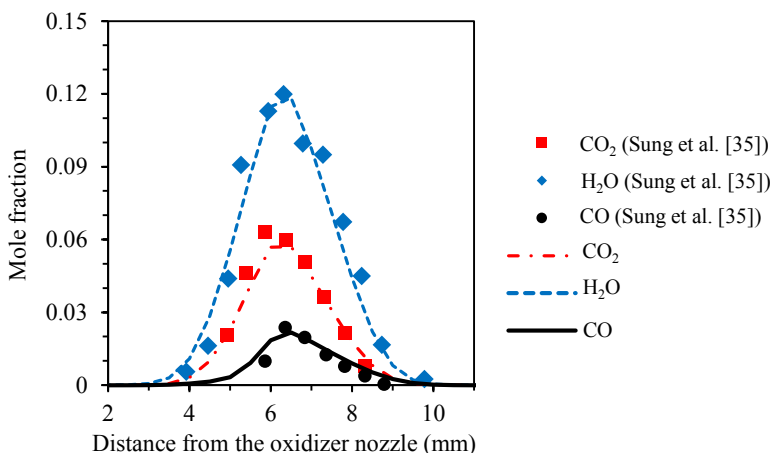
(a) Temperature, CH_4, O_2

(b) CO_2, H_2O and CO

Fig. 16. Comparison of predicted temperature and species mass fraction profiles in methane-air flames with experimental data (Sung et al. [35])

References

[1] Z. Recebli, S. Selimli, M. Ozkaymak, and O. Gonc. Biogas production from animal manure. *Journal of Engineering Science and Technology*, 10(6):722–729, 2015.

[2] S. Rasi, A. Veijanen, and J. Rintala. Trace compounds of biogas from different biogas production plants. *Energy*, 32(8):1375–1380, 2007. doi: 10.1016/j.energy.2006.10.018.

[3] O. Jonsson, E. Polman, J.K. Jensen, R. Ekund, H. Schyl, and S. Ivarsson. Sustainable gas enters the European gas distribution system. In *World Gas Conference*, Tokyo, Japan, 2003.

[4] I.U. Khan, M.H.D. Othman, H. Hashim, T. Matsuura, A.F. Ismail, M. Rezaei-DashtArzhandi, and I.W. Azelee. Biogas as a renewable energy fuel – a review of biogas upgrading, utilization and storage. *Energy Conversion and Management*, 150:277–294, 2017. doi: 10.1016/j.enconman.2017.08.035.

[5] H.O.B. Nonaka and F.M. Pereira. Experimental and numerical study of CO_2 content effects on the laminar burning velocity of biogas. *Fuel*, 182: 382–390, 2016. doi: 10.1016/j.fuel.2016.05.098.

[6] M.S. Abdallah, M.S. Mansour, and N.K. Allam. Mapping the stability of free-jet biogas flames under partially premixed combustion. *Energy*, 220:119749, 2021. doi: 10.1016/j.energy.2020.119749.

[7] L. Zhang, X. Ren, R. Sun, and Y.A. Levendis. A Numerical and experimental study on the effects of CO_2 on laminar diffusion methane/air flames. *Journal of Energy Resources Technology*, 142(8):82307, 2020. doi: 10.1115/1.4046228.

[8] T. Leung and I. Wierzba. The effect of hydrogen addition on biogas non-premixed jet flame stability in a co-flowing air stream. *International Journal of Hydrogen Energy*, 33(14):3856–3862, 2008. doi: 10.1016/j.ijhydene.2008.04.030.

[9] S. Verma, K. Kumar, L.M. Das, and S.C. Kaushik. Effects of hydrogen enrichment strategy on performance and emission features of biodiesel-biogas dual fuel engine using simulation and experimental analyses. *Journal of Energy Resources Technology*, 143(9):092301, 2021. doi: 10.1115/1.4049179.

[10] H.S. Zhen, C.W. Leung, and C.S. Cheung. Effects of hydrogen addition on the characteristics of a biogas diffusion flame. *International Journal of Hydrogen Energy*, 38(16):6874–6881, 2013. doi: 10.1016/j.ijhydene.2013.02.046.

[11] H.S. Zhen, C.W. Leung, and C.S. Cheung. A comparison of the heat transfer behaviors of biogas-H_2 diffusion and premixed flames. *International Journal of Hydrogen Energy*, 39(2):1137–1144, 2014. doi: 10.1016/j.ijhydene.2013.10.100.

[12] H.S. Zhen, Z.L. Wei, Z.B. Chen, M.W. Xiao, L.R. Fu, and Z.H. Huang. An experimental comparative study of the stabilization mechanism of biogas-hydrogen diffusion flame. *International Journal of Hydrogen Energy*, 44(3):1988–1997, 2019. doi: 10.1016/j.ijhydene.2018.11.171.

[13] M.R.J. Charest, Ö.L. Gülder, and C.P.T. Groth. Numerical and experimental study of soot formation in laminar diffusion flames burning simulated biogas fuels at elevated pressures. *Combustion and Flame*, 161(10):2678–2691, 2014. doi: 10.1016/j.combustflame.2014.04.012.

[14] Z.L. Wei, C.W. Leung, C.S. Cheung, and Z.H. Huang. Effects of H_2 and CO_2 addition on the heat transfer characteristics of laminar premixed biogas-hydrogen Bunsen flame. *International Journal of Heat Mass Transfer*, 98:359–366, 2016. doi: 10.1016/j.ijheatmasstransfer.2016.02.064.

[15] A. Mameri and F. Tabet. Numerical investigation of counter-flow diffusion flame of biogas-hydrogen blends: Effects of biogas composition, hydrogen enrichment and scalar dissipation rate on flame structure and emissions. *International Journal of Hydrogen Energy*, 41(3):2011–2022, 2016. doi: 10.1016/j.ijhydene.2015.11.035.

[16] X. Li, S. Xie, J. Zhang, T. Li, and X. Wang. Combustion characteristics of non-premixed CH_4/CO_2 jet flames in coflow air at normal and elevated temperatures. *Energy*, 214:118981, 2021. doi: 10.1016/j.energy.2020.118981.

[17] A.V. Prabhu, A. Avinash, K. Brindhadevi, and A. Pugazhendhi. Performance and emission evaluation of dual fuel CI engine using preheated biogas-air mixture. *Science of The Total Environment*, 754:142389, 2021. doi: 10.1016/j.scitotenv.2020.142389.

[18] M.H. Moghadasi, R. Riazi, S. Tabejamaat, and A. Mardani. Effects of preheating and CO_2 dilution on Oxy-MILD combustion of natural gas. *Journal of Energy Resources Technology*, 141(12):12200, 2019. doi: 10.1115/1.4043823

[19] A. Harish, H.R.Rakesh Ranga, A. Babu, and V. Raghavan. Experimental study of the flame characteristics and stability regimes of biogas – air cross flow non-premixed flames. *Fuel*, 223:334–343, 2018. doi: 10.1016/j.fuel.2018.03.055.

[20] G. Tsatsaronis, T. Morosuk, D. Koch, and M. Sorgenfrei. Understanding the thermodynamic inefficiencies in combustion processes. *Energy*, 62:3–11, 2013. doi: 10.1016/j.energy.2013.04.075.

[21] A. Datta. Entropy generation in a confined laminar diffusion flame. *Combustion Science and Technology*, 159(1):39–56, 2000. doi: 10.1080/00102200008935776.

[22] K.M. Saqr and M.A. Wahid. Entropy generation in turbulent swirl-stabilized flame: Effect of hydrogen enrichment. *Applied Mechanics and Materials*, 388:280–284, 2013. doi: 10.4028/www.scientific.net/AMM.388.280.

[23] H.R. Arjmandi and E. Amani. A numerical investigation of the entropy generation in and thermodynamic optimization of a combustion chamber. *Energy*, 81:706–718, 2015. doi: 10.1016/j.energy.2014.12.077.

[24] A.M. Briones, A. Mukhopadhyay, and S.K. Aggarwal. Analysis of entropy generation in hydrogen-enriched methane–air propagating triple flames. *International Journal of Hydrogen Energy*, 34(2):1074–1083, 2009. doi: 10.1016/j.ijhydene.2008.09.103.

[25] K. Nishida, T. Takagi, and S. Kinoshita. Analysis of entropy generation and exergy loss during combustion. *Proceedings of the Combustion Institute*, 29(1):869–874, 2002. doi: 10.1016/S1540-7489(02)80111-0.

[26] W. Wang, Z. Zuo, J. Liu, and W. Yang. Entropy generation analysis of fuel premixed CH_4/H_2/air flames using multistep kinetics. *International Journal of Hydrogen Energy*, 41(45):20744–20752, 2016. doi: 10.1016/j.ijhydene.2016.08.103.

[27] R.S. Barlow, N.S.A. Smith, J.Y. Chen, and R.W. Bilger. Nitric oxide formation in dilute hydrogen jet flames: isolation of the effects of radiation and turbulence–chemistry sub models. *Combustion and Flame*, 117(1-2):4–31, 1999. doi: 10.1016/S0010-2180(98)00071-6.

[28] J.O. Hirschfelder, C.F. Curtiss, and R.B.Bird. *Molecular Theory of Gases and Liquids*. Wiley, New York, 1954.

[29] K.K.Y. Kuo. *Principles of Combustion*. Wiley, New York, 1986.

[30] C.T. Bowman, R.K. Hanson, D.F. Davidson, W.C. Gardiner, Jr., V. Lissianski, G.P. Smith, D.M. Golden, M. Frenklach, and M. Goldenberg. GRI_Mech 2.11. Available: http://combustion.berkeley.edu/gri-mech/new21/version21/text21.html.

[31] D.N. Pope, V. Raghavan, and G. Gogos. Gas-phase entropy generation during transient methanol droplet combustion. *International Journal of Thermal Sciences*, 49(7):1288–1302, 2010. doi: 10.1016/j.ijthermalsci.2010.02.012.

[32] A.V. Mokhov, B.A.V Bennett, H.B. Levinsky, and M.D. Smooke. Experimental and computational study of C_2H_2 and CO in a laminar axisymmetric methane-air diffusion flame. *Proceedings of the Combustion Institute*, 31(1):997–1004, 2007. doi: 10.1016/j.proci.2006.08.094.

[33] J. Lim, J. Gore, and R. Viskanta. A study of the effects of air preheat on the structure of methane/air counterflow diffusion flames. *Combustion and Flame*, 121(1-2):262–274, 2000. doi: 10.1016/S0010-2180(99)00137-6.

[34] H.S. Zhen, J. Miao, C.W. Leung, C.S. Cheung, and Z.H. Huang. A study on the effects of air preheat on the combustion and heat transfer characteristics of Bunsen flames. *Fuel*, 184:50–58, 2016. doi: 10.1016/j.fuel.2016.07.007.

[35] C.J. Sung, J.B. Liu, and C.K. Law. Structural response of counterflow diffusion flames to strain rate variations. *Combustion and Flame*, 102(4):481–492, 1995. doi: 10.1016/0010-2180(95)00041-4.